ISSN 1027-4510, Journal of Surface Investigation: X-ray, Synchrotron and Neutron Techniques, 2023, Vol. 17, No. 2, pp. 392–396. © Pleiades Publishing, Ltd., 2023.
Russian Text © The Author(s), 2023, published in Poverkhnost', 2023, No. 3, pp. 92–97.

Study of the Surface Morphology of Microfluidic-Chip Channels via X-Ray Tomography and Scanning Electron Microscopy

S. V. Chapek[a], I. A. Pankin[a, *], D. V. Khodakova[b], A. A. Guda[a], A. S. Goncharova[b], and A. V. Soldatov[a]

[a] *Smart Materials International Research Institute, Southern Federal University, Rostov-on-Don, 344090 Russia*

[b] *National Medical Research Centre for Oncology, Rostov-on-Don, 344037 Russia*

**e-mail: pankin@sfedu.ru*

Received June 25, 2022; revised August 12, 2022; accepted August 12, 2022

Abstract—The visualization of microfluidic chips is considered to study the morphology of the microfluidic channel surface and estimate the quality of 3D-printing technology based on digital light processing. Visualization is performed by X-ray microtomography using different iodine-based contrast agents and by scanning electron microscopy. It is shown that X-ray microtomography visualization makes it possible to control the quality of device printing relative to the geometrical parameters of the models specified at the device prototyping stage, as well as to visualize a 3D model of microfluidic channels and surface morphology. The spatial resolution of scanning electron microscopy exceeds the print pixel size and makes it possible to clarify the presence of local defects caused by uneven solidification of the resin during sample washing.

Keywords: microfluidic systems, 3D printing, X-ray tomography, microtomography, scanning electron microscopy

DOI: 10.1134/S1027451023020039

INTRODUCTION

Microfluidics is a modern multidisciplinary research area which has grown at the intersection of physics, chemistry, biology, microhydrodynamics, microelectronics, and materials sciences. In microfluidic devices, volumes and flows of fluids are small (within the submillimeter range) which allows one to control work volumes precisely up to picolitres. These devices can be used in chemistry, medicine, pharmacy, biology, and other research-and-technology areas [1–5]. Microfluidic devices can be used for the controlled mixing of components of chemical reactions, and the separation or detection of impurities [6, 7]. Depending on their functional features, microfluidic devices can be used as microreactors [8–10], lab-on-a-chip [11–13], and organ-on-a-chip [14].

As additive technologies have been developed, conventional approaches to the preparation of microfluidic devices (micromilling, microcasting, hot stamping, and die casting), which have been believed to be "the gold standard" for 30 years, have become irrelevant. The methods mentioned above have some disadvantages, such as laborious and expensive processes and the complexity of changing the design. Moreover, "clean rooms" are frequently required which implies the corresponding complexities of production [8–10].

3D printing can dramatically change the approaches to manufacturing microfluidic devices. The following additive technologies are widely used for prototyping and producing microfluidic devices: sterEolithography (SLA), digital light processing (DLP), fused deposition modeling (FDM), and inkjet 3D printing. However, the DLP technique (a variation of steriolithography) is now preferable for the 3D printing of microfluidic devices [17–20].

To reduce the number of reactants, increase the specific surface area of mixing liquids, and decrease heating inertia, researchers strive to reduce the chip-channel diameter. At a scale of 10–100 μm, the spatial resolution of the printing method significantly affects the geometry of channels and roughness of the wall surface which, in turn, influences the hydrodynamic characteristics of liquid flows.

The conventional method of optical microscopy allows one to study the planar structure of chip channels while visualization of the internal volume of channels and investigation and investigation of channels' internal walls mortphology are complicated. The penetrating power of X-ray radiation makes it possible to study the three-dimensional structure of microfluidic channels using a proper contrast agent [21]. However, despite the extensive use of X-ray microtomography for studying the structure of microscale objects, including microchannels in various geological objects [22], this method is rarely used to visualize the channels of microfluidic devices. Thus, X-ray tomography was used in [23] to study liquid–liquid and liquid–gas

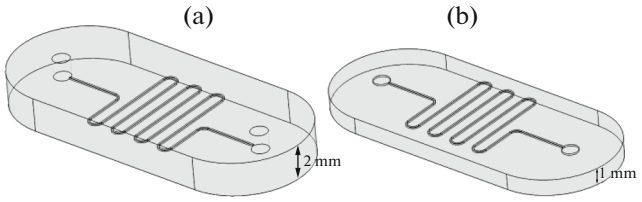

Fig. 1. 3D models of microfluidic devices in a meander geometry in the prototyping stage: (a) closed-channel chip for CT visualization and (b) open-channel chip for SEM visualization.

interfaces in thin capillary tubes (lateral section of several millimeters). Applying tomography, 3D-printed microfluidic devices with a lateral size of channels of ~400 μm were used to study the process of clot formation in blood vessels [24].

In this work, the two- and three-dimensional visualization of microfluidic devices with rectangular channels of 125 and 500 μm cross-section is carried is carried out using X-ray computer tomography with different contrast agents. The surface morphology of microfluidic channels is studied and the quality of the 3D printing of microfluidic devices is estimated. The obtained data are compared with the scanning electron microscopy (SEM) visualization of the side walls surface of microfluidic channels.

EXPERIMENTAL

3D Printing of Microfluidic Devices

A meander micromixer (Fig. 1a), which is the most widespread topology of microfluidic devices, was chosen as the model to study surface morphology of microfluidic channels. A closed-channel chip was designed and made/produced/printed/prepared for microCT studies; for the SEM study, open-channel chips were prepared (Fig. 1b). A 3D model of microfluidic devices consisting of a body and a square section channel was designed using a Fusion 360 (Autodesk, USA) CAD system. Table 1 lists the main parameters of microfluidic devices. The model was prepared for 3D printing by means of ASIGA Composer (Asiga, Australia) software. Table 2 presents the main parameters of 3D printing for both models of microfluidic devices. It should be noted that the optimal platform separation velocity was found experimentally; it affects the uniformity of the distribution of not solidified photopolymer resin inside the channel and the quality of the top surface of the microfluidic channel. An ASIGA UV MAX (Australia) 3D printer was used to obtain a microfluidic device made of FunToDo Nano clear (The Netherlands) photopolymer resin.

X-ray micro-CT Visualization

MicroCT of the chips was performed using a Quantum GX microCT (Perkin Elmer, USA) device with an X-ray tube voltage of 90 kV and current power of 88 μm. Scanning was carried out in different modes with varied resolutions. At the best resolution, the voxel size was 20 μm, the gantry rotation was 360° (the image was obtained in 427 projections), and data-accumulation time was 14 min for one measurement. To improve the contrast and quality of visualization of the boundaries, volume, and surface morphology of microfluidic channels, iodine-based contrast liquids were used: Betadine (pharmaceutically available on 10% iodine solution) and Optiray (Mallinckrodt, Canada) with an iodine concentration of 350 mg/mL (when filling the channels, Optiray was diluted with distilled water in a ratio of 1 : 10). Optiray is a contrast agent based on organically bound iodine and it is used for the microCT imaging of living organisms. The reconstruction of 3D images was conducted using

Table 1. Dimensions of the body and internal channels of the microfluidic devices specified when forming a 3D model of the device

Microfluidic-device sample	$X \times Y \times Z$ size, mm	Channel cross-section size, μm	Channel length, mm	Channel volume, mL	Covering layer
SEM	19 × 8 × 1	124	52	0.06	No
MicroCT	19 × 8 × 2	124	52	0.06	Yes
MicroCT	24 × 8 × 2	500	52	0.24	Yes

Table 2. 3D printing parameters of the studied microfluidic devices

Microfluidic-device sample	Layer height, μm	Exposure time of one layer, s	Exposure time of two layers, s	Platform-separation velocity, mm/s	UV-lamp intensity, %	Printing time, min
SEM	25	20	1	10	95	6
MicroCT	25	20	1	10	95	10
MicroCT	25	20	1	10	95	10

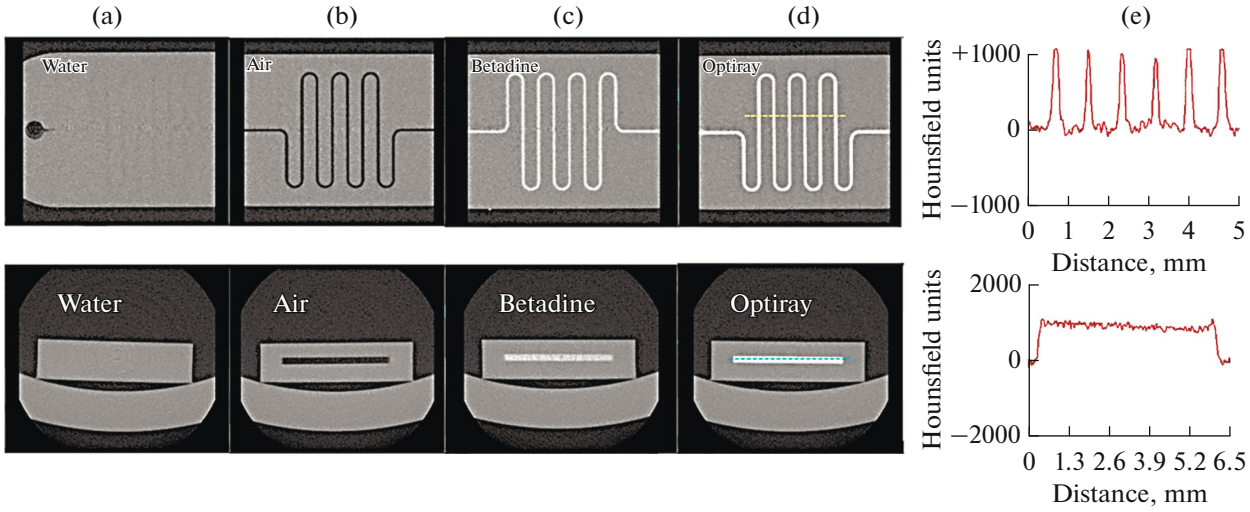

Fig. 2. 2D visualization in the top and side views for a microfluidic chip with a cross section of channels equal to 124 μm filled with: (a) distilled water, (b) air, (c) betadine, and (d) Optiray; (e) distribution of the X-ray density of a substance in a microfluidic chip filled with Optiray-based contrast agent for a series of cross sections (along the line in the top part of Fig. 2d) and the longitudinal section of the channel (along the line in the bottom part of Fig. 2d).

RadiAnt software by analysis of the set of projections obtained during microCT visualization.

Scanning Electron Microscopy

The morphology of the microfluidic channel walls was visualzied by SEM using a Teneo (FEI, USA) microscope provided by OOO SMA company. To conduct measurements, the samples were put onto a carbon tape; gold was preliminarily deposited onto the sample surface to neutralize the electrostatic charge. The microscope working chamber was evacuated to a pressure of less than 10^{-3} Pa in the high vacuum mode. The accelerating voltage and electron-beam current were 10 kV and 0.01 nA, respectively. An ETD (Everhart–Thornley detector) backscattered electron detector was used to obtain images [25].

RESULTS AND DISCUSSION

Visualization by X-ray Computer Tomography

Microfluidic devices were visualized by scanning X-ray microtomography with a voxel resolution of 20 μm. It is interesting that channels of microfluidic devices can be visualized even without a contrast agent (Fig. 2b) due to a significant difference in the radiation absorption coefficients μ of air (−1000 HU, Hounsfield units) and resin applied for 3D printing (−6.4 ± 7.1). It should be mentioned that most of the synthesis methods require the use of aqueous solutions of reagents (so-called hydrothermal synthesis). As shown in Fig. 2a, the radiation-absorption coefficients of distilled water and resin used for the printing of microfluidic devices are rather similar; therefore, the contrast is insufficient for visualization.

Next, the channel of microfluidic devices were filled with iodine-containing solutions to reach more clear visualization. Figures 2c and 2d show the results of visualization obtained when the chip was filled with betadine (alcoholic solution of iodine) and Optiray commercial contrast agent based on organically bound iodine used as contrast in clinical investigations. Figure 2e demonstrates the distribution of the X-ray density of a substance when filling the microfluidic device with Optiray-based contrast along cross (upper part) and longitudinal (lower part) sections of the channels. The given data allow one to estimate the uniformity of filling the channel with contrast agent and quantify the geometrical parameters of the studied microfluidic devices. Thus, the longitudinal section of a channel is about 6 mm and the averaged characteristic size of cross sections is ~110 ± 20 μm, which corresponds to the set-point printing parameters of microfluidic devices with a predetermined cross section of channels of 124 μm (Table 2).

Further, the 3D reconstruction of microfluidic devices with channel cross section of 124 and 500 μm filled with Optiray contrast agent was performed (Fig. 3). It can be seen that the results of microCT visualization and reconstruction of 3D images allow one to establish the features of the surface morphology of microfluidic channels. The surface of the side walls of channels with a cross section of 500 μm is more abrasive compared with the vertical surfaces, likely due to the fact that the printing resolution along the layer forming the channel side walls is 25 × 62 μm while the printing resolution along the layer forming the horizontal planes is 62 × 62 μm, i.e., a higher abrasiveness is caused by a finer printing resolution in the horizontal plane.

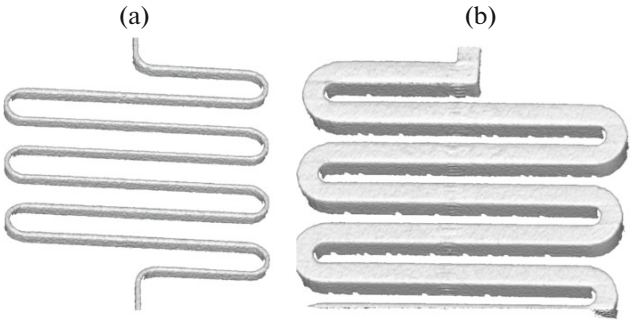

Fig. 3. Results of the 3D reconstruction of chips with cross sections of 124 (a) and 500 (b) μm filled with Optiray contrast agent. Voxel size was 20 μm for the series of two-dimensional projections used for reconstruction.

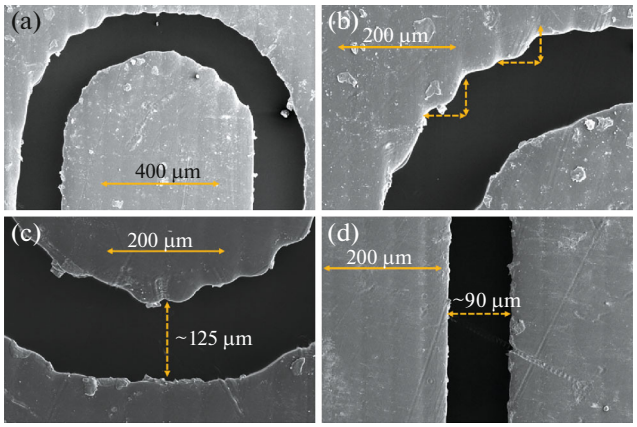

Fig. 4. SEM images of the channel side walls for microfluidic chip of meander topology: (a) channel loop, magnification 400×; (b, c) channel loop, magnification 800×; (d) straight section of the channel.

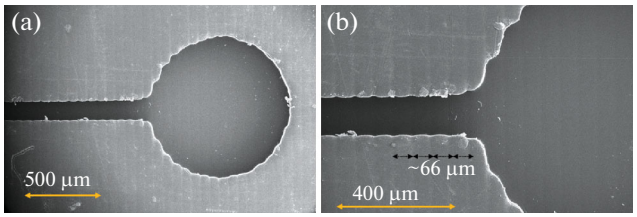

Fig. 5. SEM images of the input port of a microfluidic chip with magnifications of 200× (a) and 400× (b). Dark segments indicate print layers along the *X* axis. The average pixel size along the *X* axis is 66 μm which corresponds to the set point printing parameters (Table 2).

Visualization by SEM

Microfluidic devices with a cross-section size of 124 μm were studied by SEM. Figure 4 shows different structural units of the studied chip. As shown in Fig. 4b, the cross-section size of the straight channel part and loop region varies from 90 to 125 μm, respectively. The visualization results demonstrate a different degree of inhomogeneity of the side walls channel surface by external and internal bending radii. The arrows in Fig. 4b indicate protrusions with the size close to set point pixel size of 62.4 μm in the *XY* plane.

More and less pronounced inhomogeneities in the channel bends could be related to nonuniform rinsing (removing residual liquid resin from the channel cavity) and uneven resin solidification. This effect is clearly observed in the visualization of the input port of a round microfluidic chip (Fig. 5): the side wall on the right side of the hole seems flatter.

Some inclusions are observed in the inner part of the channel (Figs. 4a, 4c); these inclusions might be explained by both the contamination of microfluidic devices with open channels and the appearance of crystallization centers during resin solidification. From visualization of the input port (Fig 5b) inhomogeneties and microcracks are clearly seen in the side wall of the channel; the pixelated nature of the printing is also observed. An averaged pixel size along the *X* axis of ~66 μm was estimated using a SEM image at 400× magnification.

It should be noted that SEM makes it possible to conduct more detailed analysis and control of the printing quality of microfluidic chips produced by DLP 3D-printing technology. However, this technique is limited by the fact that closed-type chip must be cross-cutted, which inevitably will result in additional deformations and analysis of the walls morphologies. This will make SEM-imaging no longer objective. However, X-ray computer tomography is applicable for the visualization of closed microfluidic chips. Moreover, upon formation of stationary flows micro-CT diagnostics might be applied to study the process of microhydrodynamics and to allow 3D visualization of mixing in microfluidic channels.

CONCLUSIONS

The visualization of microfluidic chips fabricated by digital light processing 3D printing is performed by means of X-ray micro-CT tomography and scanning electron microscopy (SEM). In the first case, the structure of the channels can be visualized even without contrast agents due to sufficient contrast of the resin–air interface. MicroCT allows one to estimate the dimensions of microfluidic channels, such as the dimensions of the longitudinal and cross sections. According to the 3D reconstruction microCT images with a resolution of 20 μm, the surface of the side walls of the channels is more abrasive which can be assosiated with finer printing resolution in the vertical direction (pixel size of 25 μm along the *Z* axis) than in the horizontal one (pixel size of 62 μm along the *X* and *Y* axes). The spatial resolution of SEM images allows one to obtain detailed information about the surface

morphology of the side walls of microfluidic channels for open-channel chips and observe local printing artifacts, which are likely caused by uneven resin curing upon rinsing of microfluidic devices.

FUNDING

The study was financially supported by the Russian Ministry of Education and Science (agreement no. 075-15-2021-1363).

CONFLICT OF INTEREST

We declare that we have no conflicts of interest.

REFERENCES

1. Y. Song, H. J. Kumar, and C. S. S. R. Kumar, Small **4**, 698 (2008). https://doi.org/10.1002/smll.200701029
2. X. Lai, B. Lu, P. Zhang, X. Zhang, Z. Pu, H. Yu, and D. Li, ACS Biomater. Sci. Eng. **5**, 6801 (2019). https://doi.org/10.1021/acsbiomaterials.9b00953
3. J. Ma, S. Lee, M. Y. Yi, and C. Li, Lab Chip **17**, 209 (2017). https://doi.org/10.1039/C6LC01049K
4. E. Noviana, T. Ozer, C. S. Carrell, J. S. Link, C. McMahon, I. Jang, and C. S. Henry, Chem. Rev. **121**, 11835 (2021). https://doi.org/10.1021/acs.chemrev.0c01335
5. A.-G. Niculescu, C. Chircov, A. C. Bîrcă, and A. M. Grumezescu, Int. J. Mol. Sci. **22**, 2011 (2021). https://doi.org/10.3390/ijms22042011
6. J. Hwang, Y. H. Cho, M. S. Park, and B. H. Kim, Int. J. Precis. Eng. Manuf. **20**, 479 (2019). https://doi.org/10.1007/s12541-019-00103-2
7. S. I. Hamdallah, R. Zoqlam, P. Erfle, M. Blyth, A. M. Alkilany, A. Dietzel, and S. Qi, Int. J. Pharm. **584**, 119408 (2020). https://doi.org/10.1016/j.ijpharm.2020.119408
8. Y. Wang and M. Seidel, Sensors **21**, 2290 (2021). https://doi.org/10.3390/s21072290
9. V. Hakke, S. Sonawane, S. Anandan, Sonawane, and S. Ashokkumar, Nanomaterials **11**, 98 (2021). https://doi.org/10.3390/nano11010098
10. P. Shrimal, G. Jadeja, and S. Patel, Chem. Eng. Res. Des. **153**, 728 (2020). https://doi.org/10.1016/j.cherd.2019.11.031
11. S. Srikanth, S. Dudala, U. S. Jayapiriya, J. M. Mohan, S. Raut, S. K. Dubey, I. Ishii, and J. A. Goel, Sci. Rep. **11**, 9750 (2021). https://doi.org/10.1038/s41598-021-88068-z
12. A. Schaap, D. Koopmans, M. Holtappels, M. Dewar, M. Arundell, S. Papadimitriou, R. Hanz, S. Monk, M. Mowlem, and S. Loucaides, Int. J. Greenhouse Gas Control **110**, 103427 (2021). https://doi.org/10.1016/j.ijggc.2021.103427
13. V. Narayanamurthy, Z. E. Jeroish, K. S. Bhuvaneshwari, P. Bayat, R. Premkumar, F. Samsuri, and M. M. Yusoff, RSC Adv. **10**, 11652 (2020). https://doi.org/10.1039/D0RA00263A
14. C. Tymm, J. Zhou, A. Tadimety, A. Burklund, J. X. J. Zhang, Cell. Mol. Bioeng. **13**, 313 (2020). https://doi.org/10.1007/s12195-020-00642-z
15. L. P. Bressan, T. M. Lima, G. G. da Silveira, and J. A. F. da Silva, SN Appl. Sci. **2**, 984 (2020). https://doi.org/10.1007/s42452-020-2768-2
16. G. Gonzalez, I. Roppolo, G. F. Pirri, and A. Chiappone, Addit. Manuf. **55**, 102867. https://doi.org/10.1016/j.addma.2022.102867
17. B. M. de Costa, S. Griveau, F. Bedioui, F. Orlye, J. A. F. da Silva, and A. Varenne, Electrochim. Acta **407**, 139888 (2022). https://doi.org/10.1016/j.electacta.2022.139888
18. H. Q. Nguyen and T. S. Seo, Anal. Chim. Acta **1192**, 339344 (2022). https://doi.org/10.1016/j.aca.2021.339344
19. A. Fritschen, A. K. Bell, I. Königstein, L. Stuhn, R. W. Stark, and A. Blaeser, Biomater. Sci **10**, 1981 (2022). https://doi.org/10.1039/D1BM01794B
20. P. J. E. M. van der Linden, A. M. Popov, and D. Pontoni, Lab. Chip **20**, 4128 (2020). https://doi.org/10.1039/D0LC00767F
21. A. Jahanbakhsh, K. L. Wlodarczyk, D. P. Hand, R. R. J. Maier, and M. M. Maroto-Valer, Sensors **20**, 4030 (2020). https://doi.org/10.3390/s20144030
22. M. Kumar, M. A. Knackstedt, T. J. Senden, A. P. Sheppard, and J. P. Middleton, Petrophysics **51**, SPWLA-2010-v51n5a4 (2010). https://onepetro.org/petrophysics/article-abstract/171223/Visualizing-And-Quantifying-the-Residual-Phase?redirectedFrom=fulltext.
23. J. Schuler and N. Kockmann, AIChE J. **66**, 16890 (2020). https://doi.org/10.1002/aic.16890
24. P. F. Costa, H. J. Albers, J. E. A. Linssen, H. H. T. Middelkamp, L. van der Hout, R. Passier, A. Berg, J. Malda, and A. van der Meer, Lab. Chip **17**, 2785 (2017). https://doi.org/10.1039/C7LC00202E
25. T. E. Everhart and R. F. Thornley, J. Sci. Instrum. **37**, 246 (1960). https://doi.org/10.1088/0950-7671/37/7/307

Translated by N. Saetova